Chapter 3

Models and Techniques for Reliability Studies of Nano-scaled Interconnects

Hajdin Ceric, Houman Zahedmanesh, Roberto Lacerda de Orio, and Siegfried Selberherr

3.1. Introduction

The reliability of interconnects is affected by a complex degradation process driven by several driving forces, each of which being present from the very beginning of interconnect technology. These forces are electromigration (EM), stressmigration (SM), and thermomigration (TM). The driving forces induce a material transport in the interconnect metal, which damages the crystal structure and causes the formation of intrinsic voids. The increase of the metal resistance due to migration and growth of intrinsic voids leads finally to interconnect failure.

The thermal budget in integrated circuits (ICs) represents a problem beyond TM in interconnect metals. The heat produced by Joule heating in the interconnects in addition to the heat produced by other devices induces thermomechanical stress throughout the ICs and also affects the reliability of transistors.

Low-*k* materials have been introduced to ensure high performance of ICs with their low dielectric constant, but, unfortunately, they have brought additional thermal and mechanical problems. Low mechanical strength of low-k materials does not offer as much restraint for the degradation driving forces as sillca-based interlevel dielectric materials. Another problem with low-k dielectrics is their poor thermal conductivity which adds to the already severe thermal problems of ICs. As the thickness of interconnects decreases, the importance of material transport along grain boundaries (GBs) and interfaces increases [1-4]. Thus, the lifetime of interconnects becomes more sensitive to the values of the parameters which determine the transport, such as effective valences and diffusivities. The interconnect thickness also has an impact on the interconnect resistivity and the effective

Hajdin Ceric
Institute for Microelectronics, TU Wien, Wien, Austria

valence, which have to be considered [5, 6]. The material transport is additionally determined by the GB distribution and the orientation of single grains. The metallic microstructure in a given interconnect is influenced by the specific process conditions, choice of materials, and interconnect dimensions [7]. Improvement of the reliability for future nano-scaled interconnects can be achieved with the introduction of copper technology modifications or application of new metals as replacement for copper. Significant improvement was achieved by introducing CoWP capping layers which efficiently suppressed EM along interfaces [8, 9]. Besides CoWP, several other capping layer materials like CuSiN, CuGeN, $MnSi_xO_y$, etc. have been tested, which also improve the EM performance. Another possibility to influence the EM behavior is to change the barrier layer which covers the bottom and side walls of the copper interconnect from a typically Ti or Ta based material to Ru or its alloys etc. [10, 11]. In order to suppress EM along GBs (Fig. 3.1) dilute Cu alloys have been successfully applied. A significant reduction of material transport along the GBs has been achieved by alloying Cu with Al [12] and Mn [13-15].
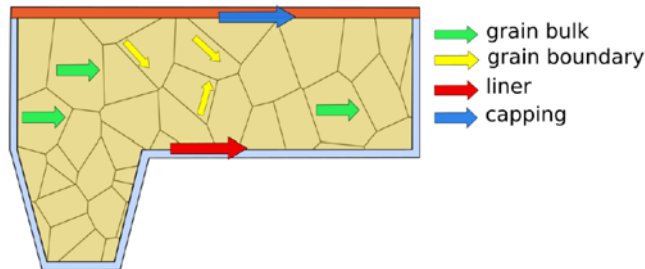

Fig. 3.1. Interconnect line with its different migration paths for material transport.

The necessity to wrap the Cu wires (in order to prevent copper migration into the neighboring dielectric) into metallic and dielectric diffusion barriers represents an additional major obstacle for scaling the dimensions of Cu interconnects below 10 nm, because the barrier itself is made of a material which has a higher resistivity than Cu. Therefore, the actual effective resistivity of the combined Cu interconnect and barrier layer is increased [10]. This barrier problem with Cu becomes even more apparent, when one considers that a practical realization of a via structure needs more barrier material than a straight interconnect line [3]. This is one of the important motivations to look for Cu replacement, besides more favorable EM properties.

To use a metal with a higher bulk resistivity than Cu, but which does not demand a barrier layer, is a preferable option [16], provided that in total it may have a similar or even lower resistivity than Cu [16]. Several metals and alloys which have potential to replace copper in the future, like Co, Ru, Ni(B) etc., have been proposed and studied in recent years [1, 3, 4, 6, 16]. Some of the metals under investigation, like Co and Ni, are magnetic. Depending on the application, the interconnect geometry, the operation frequency, and the magnetic field have to be considered.

For each metal or alloy, the prediction of the actual location of the void embryo emergence represents a challenging issue. In the case of Cu, voids nucleate inside the interconnect line either at the cap interface or at the bottom of a via or in the bulk of the interconnect metal above the via, as presented in Fig. 3.2. These different sites of void nucleation and the subsequent void dynamics lead to a multimodality of interconnect failure [17, 18].
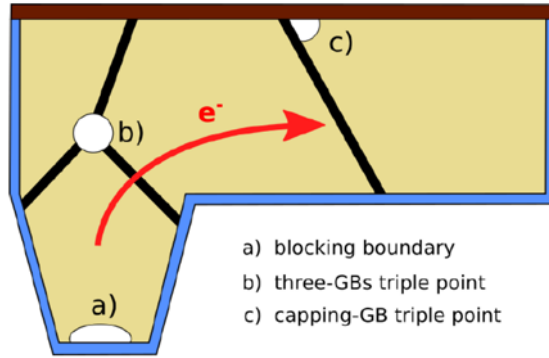

a) blocking boundary
b) three-GBs triple point
c) capping-GB triple point

Fig. 3.2. Three characteristic void nucleation sites inside a dual-damascene interconnect.

3.1.1. Black's Equation

Since its publishing, Black's equation [19] is a widespread and a very popular mathematical basis for modelling and predicting interconnect failure behavior. It expresses a median interconnect time-to-failure, t_{MTTF}, in dependence of the following three parameters: the pre-exponential A coefficient, the current exponent n, and the activation energy E_a.

$$t_{MTTF} = \frac{A}{j^n} exp\left(-\frac{E_a}{kT}\right) \tag{3.1}$$

Particularly important here is the activation energy E_a, because this parameter has the largest impact on the predicted median interconnect time-to-failure (MTF), as we can see from (3.1). If we consider the physics of EM induced transport, it becomes clear that the activation energy as used in (3.1) is a result of the cumulative effect of several different activation energies related to the various different migration paths. For a complete picture of EM degradation, at least the following migration paths must be considered:

- Grain bulk;
- Barrier layer;
- Capping layer;
- Grain boundaries.

Each of these migration paths is characterized its own diffusion coefficient which depends on the particular diffusion coefficient pre-exponential and on the particular activation

energy. Generally speaking, the cumulative activation energy, as used in (3.1), is not only a function of the activation energies of each of the above-mentioned migration paths, but also a function of the interconnect's layout geometry and microstructure.

3.1.2. Beyond Black's Equation

The cumulative activation energy, E_a, is routinely determined during EM tests and the knowledge of its value is quite useful for the prediction of interconnect lifetimes, but rather problematic, if one wants to study in detail the particular degradation mechanism which leads to the EM failure itself. The crucial question is to which extent each of the activation energies of the different acting migration paths actually contributes to the cumulative activation energy. The importance of this question becomes obvious, if one considers some new material for the capping or the barrier layer, or to modify the copper electro-deposition process in such a way that it influences the copper microstructure. In such a case, the real impact of the technological change must be estimated. There are two ways how this can be done. The first one is experimentally, where a dedicated measurement setup is used to estimate the activation energy of the new capping and barrier interface. The second approach is the application of simulation using physics-based models. This approach provides not only a far more comprehensive understanding of the impact of new materials, but also offers a deeper insight, how the whole degradation process leading to the failure unfolds.

3.2. The Physics-BASED Modelling of Electromigration

Physics-based modelling of EM uses the framework [20], which represents a further development from the original work of Sarychev and Zithnikov [21]. According to this modelling approach, the lifetime of an interconnect structure t_f consists of a void nucleation time t_N and a void evolution time t_E, corresponding to two failure development phases.

$$t_f = t_N + t_E \tag{3.2}$$

Each of these two phases demands its own modelling effort.

The central governing equations of EM models are the vacancy flux equation (3.3) and the vacancy balance equation (3.4).

$$\vec{J_v} = D_{\text{eff}} \left(\frac{C_v}{kT} |Z_{\text{eff}}^* e| \rho \vec{j} + \frac{C_v}{kT} f \Omega \nabla p - \nabla C_v \right), \tag{3.3}$$

$$\frac{\partial C_v}{\partial t} = -\nabla \cdot \vec{J_v} + G_{\text{eff}}(C_v), \tag{3.4}$$

where D_{eff} is the local diffusivity, C_v is the vacancy concentration, p is the hydrostatic stress, ρ is the interconnect resistivity, $\vec{j}$ is the current density, Ω is the atomic volume, and f is the atom-vacancy relaxation factor. G_{eff} is the Rosenberg-Ohring recombination

term and Z_{eff}^* is the effective valence. In order to reproduce realistic mechanical conditions, all materials in the structure and their corresponding properties must be included in the modelling framework. Both the void nucleation model, as well as the void evolution model, are solved simultaneously with the equations of mechanics [21].

$$\frac{\partial \varepsilon_{ij}^v}{\partial t} = \frac{1}{3}\left[(1-f)\nabla \cdot \vec{J_v} + f G_{\text{eff}}(C_v)\right]\delta_{ij},$$
(3.5)

$$\nabla \cdot \sigma = 0, \quad \sigma = E(\varepsilon - \varepsilon^v - \varepsilon^{th}),$$
(3.6)

where E is the the fourth-order elasticity tensor, ε^v is the volumetric strain component which rises due to EM, and ε^{th} represents the impact of thermal loads.

From the stress tensor σ, the normal stresses at all interfaces and GBs can be obtained. The *void nucleation phase* ends, when one of the normal stresses surmounts the local critical stress threshold σ_{crit}, which is discussed in the next sections. The time needed for the critical stress threshold to be reached is the void nucleation time t_N.

3.2.1. Blech's Equation

The dynamics of the vacancy flux $\vec{J_v}$, plays a crucial role in the development of EM failure. When for $\vec{J_v} = 0$ the stress equilibrium state is achieved (cf. Fig. 3.3) for a back-flow stress which is lower than the critical stress-threshold needed for void nucleation, the interconnect is virtually "immortal" (arbitrarily long-living). This situation corresponds to the generalization of the one-dimensional Blech effect.
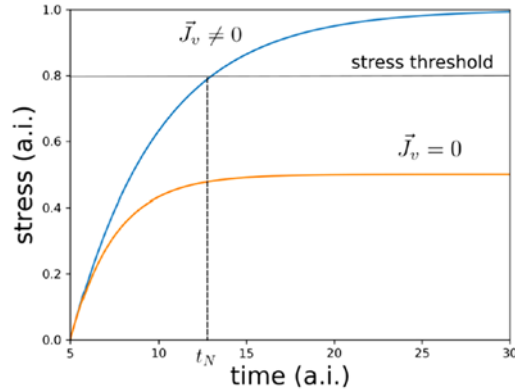

Fig. 3.3. Stress dynamics depending on the zero-flux condition.

If one assumes that the pressure and vacancy concentration are in a local equilibrium [20]

$$C_v = C_v^0 exp\left(W_f - \frac{\Omega p}{kT}\right),$$
(3.7)

where W_f is the interaction energy between the vacancy and the stress field and C_v^0 is the vacancy concentration in the absence of any stress effects, the Blech's condition follows directly from the zero-flux condition $(\vec{J_v} = 0)$, by inserting (3.7) into (3.3). One obtains for a one-dimensional linear interconnect of length l

$$j_x l = \frac{\Omega(1+f)\Delta\sigma_x^{eq}}{\rho|Z_{eff}^*e|} = \frac{\Omega(1+f)|\sigma_x(l) - \sigma_x(0)|}{\rho|Z_{eff}^*e|}, \tag{3.8}$$

where $p = -\sigma_x$ and $\sigma_x(l)$ and $\sigma_x(0)$ are the stresses at both ends of the linear interconnect. When the zero-flux condition is attained for a certain back-stress which is higher than the critical-stress needed for void nucleation, a void embryo is formed.

3.2.2. Effective Valence and Resistivity

The bulk effective valence Z_{bulk}^*, and the resistivity ρ are related on a fundamental physical level, because both parameters characterize different aspects of electron scattering in a current carrying metal [22].

$$Z_{bulk}^*(T) = Z_d + Z_w(T) = Z_d + \frac{K}{\rho(T)}, \tag{3.9}$$

where Z_d is the direct valence which is assumed to be equal to the bare valence of Cu, and K is the proportionality factor which has been fitted for Z_{bulk}^* for a thick interconnect at room temperature. Various advanced models can be used for modeling the interconnect resistivity [23].

Because on average, there are fewer atoms inside the GBs than in the bulk, the GB region presents a repulsive potential to the electrons. Consequently, the electron wind force in the GB region is lower than in the bulk. As shown by Sorbello [24] even for a low GB potential (1/10 of the Fermi energy), the wind force inside the GB is about 20 % smaller than in its immediate vicinity outside the GB.

3.2.3. Conditions for Void Nucleation

The conditions for void nucleation are determined by either the geometrical and/or the microstructural features of the interconnect metal and layout. One particular geometrical feature can hinder vacancy flux and thus cause a local increase in the concentration of vacancies, which in turn leads to a local increase in the tensile mechanical stress. After a certain stress-threshold is attained, an initial void is nucleated [25, 26]. A microstructural feature, such as a GB, can also lead to a local disturbance of material transport and to a subsequent rise in tensile stress at so-called triple points (an intersection of a GB with an interface). The absolute critical value of stress σ_{crit} can be expressed as

$$\sigma_{crit} = \left(\frac{kG_cB}{h_{Cu}}\right)^{1/2}, \tag{3.10}$$

where G_c is the interface energy per unit area related to the top interface of the line between Cu and the cap layer. B denotes the confinement/effective modulus, h_{Cu} denotes the height of the line, and k is a calibration parameter. All parameter values are set according to previous works [27, 28].

3.3. Modelling of the Microstructure

The microstructure of Cu interconnects generally depends on the technological process, the interconnect geometry, and the choice of surrounding materials. Different choices of materials for barrier and cap layers may influence properties of the microstructure [28]. There are several studies dealing with the impact of the Cu microstructure on the EM failure behavior [29, 30]. They describe, how the GBs distribution and the texture inside single grains influence the interconnect failure and the failure time distribution. For a complete modelling of the microstructure, besides a description of the grain crystallography, an appropriate understanding of the GB physics is a necessity. The following three aspects of GB physics must be considered [31]:

- The GB as a fast diffusivity path;

- The GB as a site of vacancy production and annihilation;

- The GB as an obstacle to material transport.

In the case of typical microstructures for small interconnects, two additional aspects must be considered. First, the microstructure strongly depends on the interconnect width and second, due to the increased temperatures during operation, the microstructure may undergo transformations. Experimental SEM/FIB/EBSD [32-35] studies of interconnects' microstructures provide the grain size distribution and the crystal orientations inside grains. The studies show that the grain sizes inside Cu interconnects are distributed according to the lognormal distribution and tend to have several predominant crystal orientations [34]. An "effective values" approach has been used for a long time to model the cumulative effect of different atomic transport paths on the overall diffusivity. The main advantage of this approach is its simplicity, because one basically needs only the geometrical dimensions of the interconnect line and some characteristics of the microstructure to calculate an effective value of diffusivity and effective valence. The GB volume fraction ϵ_p dependent effective values of the Rosenberg-Ohring term G_{eff}, the effective valence Z_{eff}^*, and the effective diffusivity D_{eff}, are given by the following terms, respectively [27]:

$$G_{\text{eff}}(C_v) = -\left(C_{eq} - C_v\right)\left(\frac{1 - \epsilon_p}{\tau_{\text{bulk}}} + \frac{\epsilon_p}{\tau_{gb}}\right), \tag{3.11}$$

$$Z_{\text{eff}}^* = Z_{\text{bulk}}^*\left(1 - \epsilon_p\right) + Z_{gb}^*\epsilon_p, \tag{3.12}$$

$$D_{\text{eff}} = D_{\text{bulk}} + D_{\text{lin}}\left(\frac{2}{w} + \frac{1}{h}\right)\delta_{\text{I-lin}} + D_{\text{cap}}\frac{\delta_{\text{I-cap}}}{h} + \epsilon_p D_{gb}, \tag{3.13}$$

where h is the interconnect height and w is the interconnect width. Each transport path is characterized by its diffusivity and its thickness: bulk (D_{bulk}, h), cap layer (D_{cap}, $\delta_{I\text{-}cap}$), and liner (D_{lin}, $\delta_{I\text{-}lin}$).

Equations (3.11), (3.12), and (3.13) can be directly used for parametrization of the vacancy dynamics model given by equations (3.3) and (3.4). However, this type of "cumulative" microstructure description is inadequate to capture microstructural features important for interconnect reliability. A model which is able to capture all the relevant microstructural aspects requires a detailed description of the vacancy dynamics at a single GB as introduced in [31].

For the implementation in the GB plane (Fig. 3.4), the model is described by the Rosenberg-Ohring term

$$G_g = -\frac{1}{\tau_g}\left(C_v^{eq} - C_v^{im} \left(1 - \frac{2\omega_R}{\omega_T(C_{v1} + C_{v2})} \right) \right), \tag{3.14}$$

and a segregation condition at the GB, which regulates the vacancy transport from the Grain 1 to the Grain 2.

$$J_{12} = \omega_T\left(C_v^{eq} - C_v^{im} \right)(C_{v1} - C_{v2}), \tag{3.15}$$

where C_{v1} and C_{v2} are the vacancy concentrations in Grain 1 and Grain 2, respectively, ω_T is the vacancy-trapping rate, ω_R is the vacancy release rate, C_v^{im} is the concentration of vacancies trapped in the GB, C_v^{eq} is the equilibrium vacancy concentration, and τ_{gb} is the vacancy recombination rate. The model is complete with the diffusivity D_{GB} in the GB plane. The detailed GB model, combined with the vacancy dynamics equations (3.2) and (3.3), produces pile-ups of vacancies at triple points in three-dimensional microstructures, as shown in Fig. 3.5. The corresponding peaks of the mechanical stress are presented in Fig. 3.6.
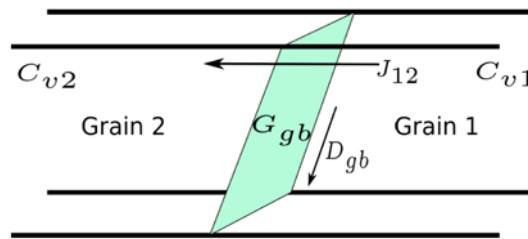

Fig. 3.4. Schematic picture of the two-dimensional GB plane.

The detailed GB model can be applied at the surface of an arbitrary shape defining the GB between two adjacent grains. The only condition is an appropriate FEM discretization of the surface.
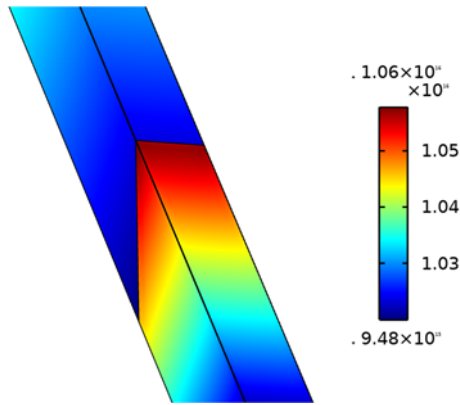
Fig. 3.5. Increase of the vacancy concentration (1/cm³) close to a triple point along the capping layer. The locations of the peak vacancy concentrations correspond to the peaks of the tensile stress.
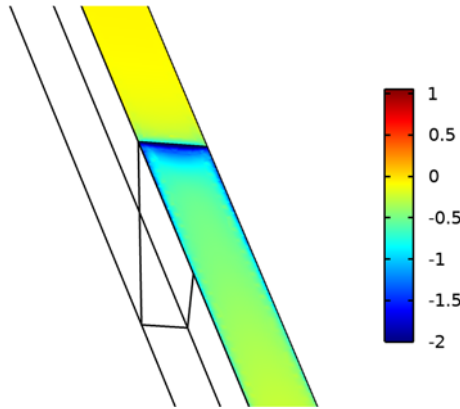

Fig. 3.6. Peak of mechanical stress (MPa) close to a triple point along the capping layer.

3.4. Analytical Model for Void Growth

In order to estimate the duration of the second phase of failure development, it is necessary to predict the void growth velocity. The normal velocity v_n of the void surface is calculated according to [20].

$$v_n = \Omega(\vec{J}_v \cdot \vec{n} - \nabla \cdot \vec{J}_s) \tag{3.16}$$

From (3.16) it can be seen that the void surface evolves due to the vacancy transport in the normal direction, $\vec{J}_v \cdot \vec{n}$, and the divergence of the surface vacancy flux, $\nabla \cdot \vec{J}_s$ (Fig. 3.7). The surface vacancy flux $\vec{J}_s$ itself rises due to the tangential component of the current density $\vec{j}_t$ and the surface gradient of the chemical potential μ_s.

$$\vec{J_s} = -\frac{D_s\delta_s}{kT\Omega}\left(|Z_s^*e|\rho\vec{j_t} + \nabla_s\mu_s\right), \tag{3.17}$$

where D_s is the surface diffusivity and δ_s is the thickness of the diffusion surface. The surface chemical potential μ_s is given as

$$\mu_s = \Omega(W_s - \gamma_s\kappa) \tag{3.18}$$

where γ_s is the surface energy, κ is the local curvature of the surface, and $W_s = (\sigma:\varepsilon)/2$ is the local elastic strain energy density. From (3.16)-(3.18) follows that there are four components of the surface velocity: the elastic strain energy velocity component v_n^s, the EM velocity component v_n^e, the surface free energy velocity component v_n^f, and the vacancy absorption velocity component v_n^v.

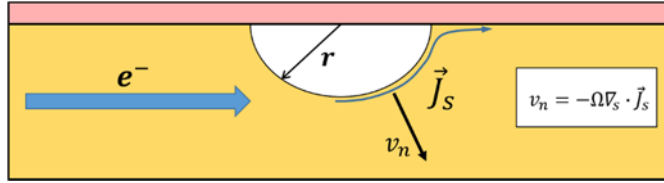$$v_n = v_n^s + v_n^e + v_n^f + v_n^v \tag{3.19}$$

Fig. 3.7. Atom migration along the void surface and the resulting normal velocity.

We assume that the void possesses throughout its growth a half-cylindrical shape and that the EM velocity component (v_n^e) dominates over the other three velocity components.

$$v_n^e = \frac{D_s\delta_s\rho|Z_s^*e|}{kT}\nabla_s\vec{j_t} \tag{3.20}$$

The lower limit (the worst case) of the void evolution time t_E is obtained by assuming that the whole void of radius r grows with the maximum velocity at its surface, $v_n^{max}(r)$ [27].

$$t_E = \int_{r_0}^{r_c}\frac{dr}{v_n^{max}(r)} \tag{3.21}$$

Here, the critical void radius r_c is the solution of the equation

$$R_{failure} = R_{total}(r_c), \tag{3.22}$$

where $R_{failure}$ is the predefined failure resistance (usually 20 % of the nominal interconnect resistance) and $R_{total}(r_c)$ is an analytical function estimating the resistance of an interconnect containing a half-cylindirical void with radius r_c. The initial radius of a void r_0 is estimated based on the local pressure distribution near the triple point, where the void is assumed to emerge (see Section 3.5).

Even in case of a fully three-dimensional simulation, due to the assumption of a half-cylindrical void, the tangential component of the current density $j_t(r,\theta)$ can be estimated for all void sizes and interconnect thicknesses h ($= 2w$) as

$$j_t(r,\theta) = \frac{j_0 h \sin\theta}{h - r \sin\theta} q(r), \tag{3.23}$$

where j_0 is the current density far away from the void surface (in a region unperturbed by the presence of a void) and the angle θ (cf. Fig. 3.8) determines the position on the void surface. $q(r)$ is an additional fitting function [36] introduced to closely match the analytical surface velocity calculations with those calculated with COMSOL Multiphysics [37].

$$q(r) = \sum_{i=0}^{n} (-1)^i \left(\frac{r}{h}\right)^{2i} \tag{3.24}$$

By substituting (3.24) in (3.23) and then (3.23) in (3.20), the following expression is obtained:

$$v_n(r,\theta) = \frac{D_s \delta_s \rho |Z_s^* e|}{kTr} \frac{d j_t(r,\theta)}{d\theta}, \tag{3.25}$$

The comparison of analytical surface normal velocity calculations (3.25) and COMSOL Multiphysics calculations for $h = 2w = 46$ nm and a current density $j = 1.0$ MA/cm² for two different void sizes ($r_1 = 0.6h$ and $r_2 = 0.8h$) and for a typical operating condition temperature of 100 °C is shown in Fig. 3.9. Since the worst case scenario is of interest, i.e., void growth with the maximum surface velocity, for the estimation of the void evolution time t_E in (3.21) the following expression is used:

$$v_n^{max}(r) = \frac{D_s \delta_s \rho |Z_s^* e|}{kTr} \max_{0 \le \theta \le \pi} v_n(r,\theta), \tag{3.26}$$
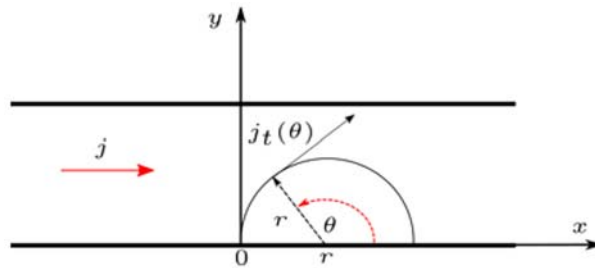

Fig. 3.8. Structure used in the derivation of equation (3.23).

3.5. Estimation of Initial Void Size

After an initial void is formed, the previously built stress ($p(x,y,z)$) relaxes. The volume of the initial void is determined as

$$V_0 = -\frac{1}{B} \int_V p(x,y,z) \, dx \, dy \, dz \qquad (3.27)$$

In order to simplify the model implementation, it is assumed that a cylindrical void is formed around the triple point and spans the entire interconnect width w. This assumption allows for the calculation of the initial void radius r_0.

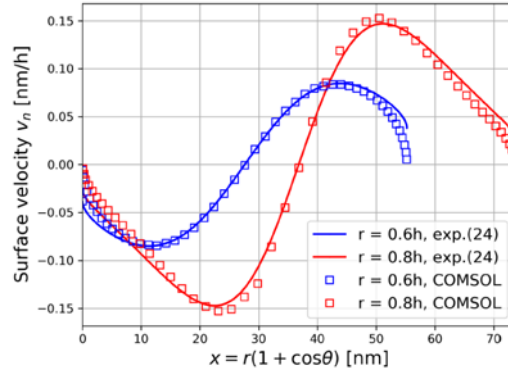$$r_0 = \sqrt{\frac{2V_0}{\pi w}} \qquad (3.28)$$

Fig. 3.9. Comparison between analytically calculated surface normal velocity using (3.25) with FEM calculation performed in COMSOL Multiphysics for 100 °C and for a current density $j = 1.0$ MA/cm².

3.6. Resistance Calculation

An increase of the interconnect resistance leads to interconnect failure. The resistance increase is caused by the emergence, subsequent growth, shape change, and movement of intrinsic voids. The evolving void surface can be modelled with different levels of accuracy, but more accurate modelling is always more computationally demanding. For the sake of simplicity and speed of calculation, we use three-dimensional void shapes with a simple geometrical basis, like a half-circle and a half-ellipse.

The resistance of an interconnect segment containing a cylindrical void with elliptical basis (*2a* and *2b* are the minor and major axes, respectively, cf. Fig. 3.10) is

$$R_0(a,b) = \frac{a\rho}{bw}\left[\pi\left(\frac{h}{s} - 1\right) + \frac{2h}{s} arctan\left(\frac{b}{s}\right)\right], \qquad (3.29)$$

with $s = (h^2 - b^2)^{1/2}$. The total resistance $R_{total}(a,b)$ for a void placed in a straight interconnect line is calculated according to the equivalent circuit presented in Fig. 3.11:

$$\frac{1}{R_{total}(a,b)} = \frac{1}{R_{cap}} + \frac{1}{R_{lin}} + \frac{1}{R_{metal}(a,b)}, \qquad (3.30)$$

$$R_{metal}(a,b) = 2R_2(b) + R_0(a,b), \tag{3.31}$$

$$R_2(b) = \frac{\rho_{metal}(1-2b)}{2wh}, \tag{3.32}$$
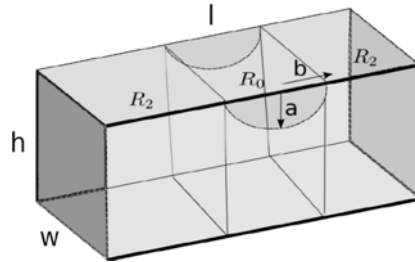

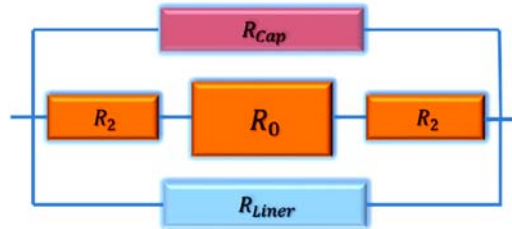**Fig. 3.10.** Structure used in the derivation of equation (3.29).

Fig. 3.11. Replacement schema for a segment of an interconnect containing a cylindrical void. The resistances of the cap layer, R_{cap}, and of the liner, R_{lin}, are included.

With the expressions (3.21) and (3.25), and the resistance calculation based on (3.30), the dependence of the void growth time on the interconnect dimensions can be determined. Fig. 3.12 shows the resistance increase for a 1 μm long and 23 nm wide interconnect section for three different temperatures and a current density $j = 1.0$ MA/cm^2.

3.7. Overall Scheme

In order to estimate the interconnect lifetime (t_f), both the void nucleation (t_N), as well as the void evolution time (t_E) must be estimated as accurately as possible. The complete simulation scheme utilized in this work is presented in Fig. 3.13. As one can see, the overall simulation procedure is divided into two parts: estimation of t_N (void nucleation time), which is performed numerically by application of the FEM, and the estimation of t_E (void evolution time), which is carried out analytically. The equation system solved in the FEM part of the simulation consists of equations (3.3)-(3.6) together with the Laplace equation for the electric field (cf. Fig. 3.13). The solution of the Laplace equation provides the distribution of the current density j inside the metallization, which is needed for solving the vacancy balance equations (3.3) and (3.4).
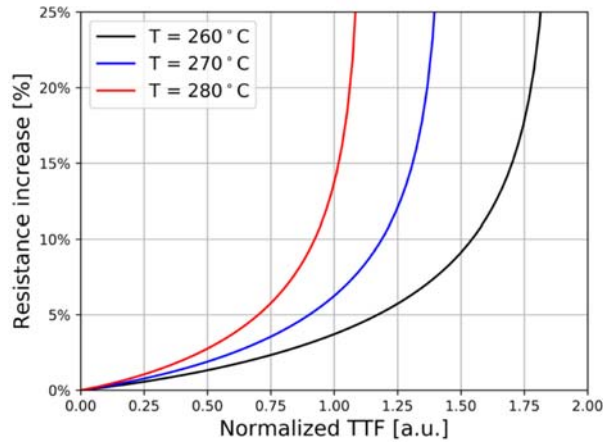
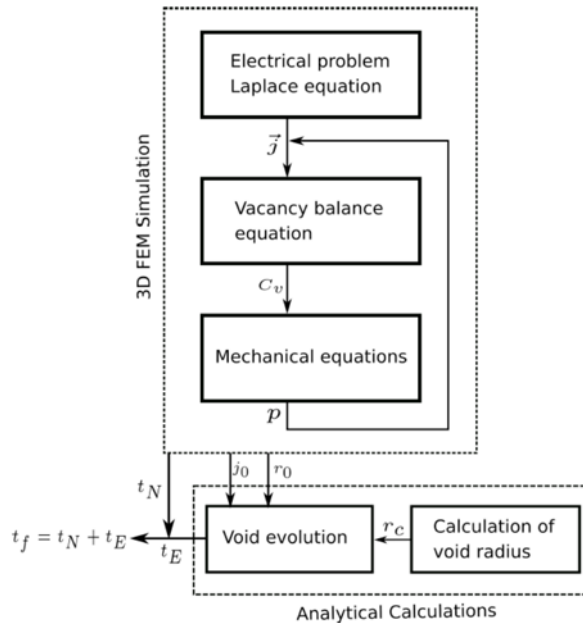**Fig. 3.12.** Resistance change for three different temperatures.

Fig. 3.13. Overall two-part simulation scheme. The void nucleation time is determined in the "3D FEM Simulation" part and the void evolution time in the "Analytical Calculations" part.

The solution of the vacancy balance equations determines the vacancy concentration C_v throughout the metal bulk. The redistribution of vacancies, driven by EM and the accompanying forces, gives rise to mechanical stress calculated by simultaneously solving equations (3.5) and (3.6). The vacancy balance equation and the mechanical equations are solved in a time loop, until the critical stress is reached at some triple point at the capping layer. This event also marks the end of the 3D FEM part of the simulation flow. The results from the 3D FEM solution, which are carried over to further processing are: the void

nucleation time t_N, the current density j_0, and the radius of the initial void r_0. The current density j_0 and the void radius r_0 are needed for the calculation of the void evolution time. The critical void radius r_c is obtained by solving equation (3.22).

3.8. Simulation Results and Discussion

The modelling framework described above is used to study the *failure time* dependence on:

a) Interconnect thickness;

b) Mechanical and material transport properties of SiN_x and Co caps.

COMSOL Multiphysics [37] was used for the simulations. The 1 µm long Cu interconnect is placed between two contacts and encapsulated in a Ta barrier layer on all sides except the top, which is covered with the cap layer. The Cu interconnect with all interface layers is fully embedded in SiO_2 (cf. Fig. 3.14). Typical material properties for all involved materials and interfaces are assumed, including a stress threshold of 20 MPa stress threshold for void nucleation at the SiN_x cap and of 30 MPa at the Co cap. The interface diffusivity at the SiN_x/Cu interface is assumed to be 100 times higher than at the Co/Cu interface. The temperature for the simulations is set at 300 °C. The detailed modelling approach allows for the observation of different physical characteristics as the failure develops.
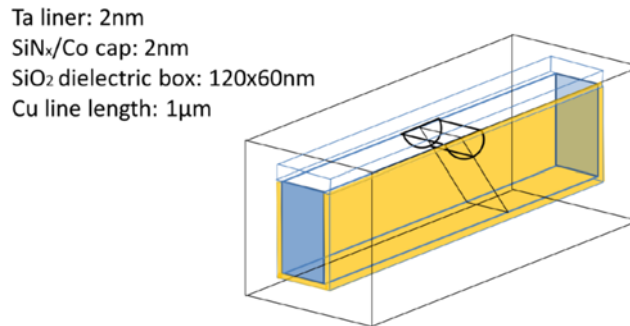

Ta liner: 2nm
SiN_x/Co cap: 2nm
SiO_2 dielectric box: 120x60nm
Cu line length: 1µm

Fig. 3.14. Structure used for simulations. A cylindrical void nucleation is assumed at the triple point.

As one can see from (3.21), an estimation of the void evolution time (t_E) demands the extraction of the function $v_n^{max}(r)$, which can be studied in detail by the simulation results presented in Fig. 3.15, obtained by the overall simulation schema discussed in Section 3.7.

The interconnect lifetimes for both types of capping layers are significantly reduced for a thinner interconnect (cf. Table 3.1), but the benefit of replacing SiN_x with Co is clearly recognizable. This behavior is confirmed by numerous experimental results (e.g. [3, 16, 27, 38]), as expected, because for thinner interconnects a larger portion of atoms is

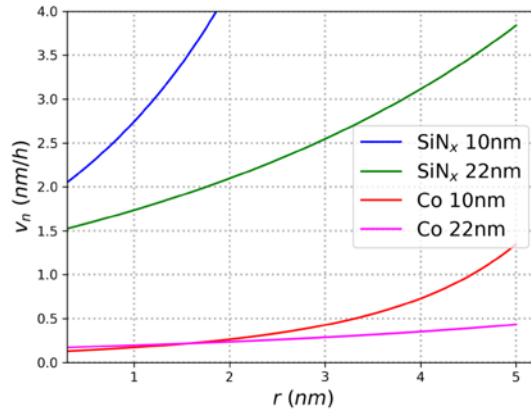transported along the interfaces and a smaller void volume is sufficient to produce the fatal failure.

Fig. 3.15. Normal velocity (v_n) of the void surface in dependence on the void radius (r) for SiN_x and the Co cap.

Table 3.1. Lifetime dependence on interconnect thickness. All failure times are normalized to the t_F, the failure time of a 22 nm wide interconnect with a SiN_x cap.

Capping	Thickness [nm]	t_N/t_F	t_E/t_F	t_f/t_F
SiN_x	10	0.200	0.099	0.299
SiN_x	22	0.395	0.605	1.000
Co	10	0.304	1.598	1.902
Co	22	0.608	5.379	5.987

3.9. Conclusion

By reducing the width of interconnects to 10 nm and below, while at the same time considering Cu-replacement metals, interconnect reliability studies are on the verge of entering uncharted territory for the first time in more than 20 years. While experimental methods for the analysis of interconnect failures have been gradually improved and refined, mathematical models, which were directly applied for study of experimental results, have remained to a large part basically one-dimensional models. These models inevitably rely on effective and average properties of crucial parameters, e.g. diffusivity, and mostly ignore explicit three-dimensional features, which indubitably influence these parameters. As we know today, the reliability of downscaled interconnect increasingly depends on the atomic migration along interfaces, whereas the interconnect metal microstructure plays an important role and thus must be addressed accordingly. To meet the challenges of current and future interconnect reliability, an application of advanced physically based models is a necessity. The development of these models took place in parallel to the development of advanced experimental methods, but they have never been

fully utilized for the study of experimental results. We presented an EM reliability model which considers different effects related to the narrowness of the interconnect, as well as to the particular material choice needed for a layout realization. Among the particular effects taken into account are the effective valence dependence on the microstructure and interconnect thickness, the effects of interfacial EM paths, and void growth under the assumption of a narrow interconnect. The dependence of interconnect lifetimes on length, thickness, and the diffusivities of the cap layers obtained by simulation fully match known and published results.

References

[1]. H. Zahedmanesh, Z. Tökei, K. Croes, Investigating the electromigration limits of Cu nano-interconnects using a novel hybrid physics-based model, *J. Applied Physics*, Vol. 126, Issue 5, 2019, 055102.

[2]. S. Choi, C. Christiansen, L. Cao, J. Zhang, R. Filippi, T. Shen, K. B. Yeap, S. Ogden, H. Zhang, B. Fu, P. Justison, Effect of metal line width on electromigration of BEOL Cu interconnects, in *Proceedings of the International Reliability Physics Symposium (IRPS'18)*, 2018, pp. F.4.1-F.4.6.

[3]. F. Griggio, J. Palmer, F. Pan, N. Toledo, A. Schmitz, I. Tsameret, R. Kasim, G. Leatherman, J. Hicks, A. Madhavan, J. Shin, J. Steigerwald, A. Yeoh, C. Auth, Reliability of dual-damascene local interconnects featuring Cobalt on 10 nm logic technology, in *Proceedings of the International Reliability Physics Symposium (IRPS'18)*, Vol. 1, 2018, pp. 6E.3-1-6E.3-5.

[4]. C.-K. Hu, J. Kelly, H. Huang, K. Motoyama, H. Shobha, Y. Ostrovski, J. H.-C. Chen, R. Patlolla, B. Peethala, P. Adusumilli, T. Spooner, R. Quon, Future on-chip interconnect metallization and electromigration, in *Proceedings of the International Reliability Physics Symposium (IRPS'18)*, 2018, pp. 4F.1-1-4F.1-6.

[5]. I. Ciofi, P. J. Roussel, Y. Saad, V. Moroz, C.-Y. Hu, R. Baert, K. Croes, A. Contino, K. Vandersmissen, W. Gao, P. Matagne, M. Badaroglu, C. J. Wilson, D. Mocuta, Z. Tökei, Modelling of via resistance for advanced technology nodes, *IEEE Trans. Electron Devices*, Vol. 64, Issue 5, 2017, pp. 2306-2313.

[6]. J. S. Chawla, S. H. Sung, S. A. Bojarski, C. T. Carver, M. Chandhok, R. V. Chebiam, J. S. Clarke, M. Harmes, C. J. Jezewski, M. J. Kobrinski, B. J. Krist, M. Mayeh, R. Turkot, H. J. Yoo, Resistance and electromigration performance of 6 nm wires, in *Proceedings of the International Interconnect Technology Conference (IITC'16)*, 2016, pp. 63-65.

[7]. L. E. Spinella, The scaling and microstructure effects on the thermal stress and reliability of through-silicon vias in 3D integrated circuits, PhD Thesis, *The University of Texas at Austin*, 2017.

[8]. E. Zschech, H. J. Engelmann, M. A. Meyer, V. Kahlert, A. V. Vairagar, S. G. Mhaisalkar, A. Krishnamoorthy, M. Yan, K. N. Tu, V. Sukharev, Effect of interface strength on electromigration induced inlaid copper interconnect degradation: Experiment and simulation, *Zeitschrift für Metallkunde*, Vol. 96, Issue 9, 2005, pp. 966-971.

[9]. E. Zschech, M. A. Meyer, S. G. Mhaisalkar, A. V. Vairagar, A. Krishnamoorthy, H. J. Engelmann, V. Sukharev, Effect of interface modification on EM-induced degradation mechanisms in copper interconnects, in *Proceedings of the International Conference on Materials for Advanced Technologies (ICMAT'05)*, Vol. 504, Issues 1-2, 2005, pp. 279-283.

[10]. Z. Tökei, K. Croes, G. P. Beyer, Reliability of copper low-*k* interconnects, *Microelectron. Reliab.*, Vol. 87, 2010, pp. 348-354.

[11]. K. Croes, S. Demuynck, Y. K. Siew, M. Pantouvaki, C. J. Wilson, N. Heylen, G. P. Beyer, Z. Tőkei, Full reliability study of advanced metallization options for 30 nm 1/2 pitch interconnects, *Microelectron. Eng.*, Vol. 106, 2013, pp. 210-213.

[12]. A. O. Oates, Strategies to ensure electromigration reliability of Cu/Low-*k* interconnects at 10 nm, *ECS J. Solid State Science Techn.*, Vol. 4, Issue 1, 2015, pp. N3168-N3176.

[13]. L. Cao, P. S. Ho, P. Justison, Electromigration reliability of Mn-doped Cu interconnects for the 28 nm technology, in *Proceedings of the International Reliability Physics Symposium (IRPS'13)*, 2013, pp. EM.5.1-EM.5.4.

[14]. M. H. Lin, A. S. Oates, Electromigration in dual-damascene CuMn alloy IC interconnects, *IEEE Trans. Device Materials Reliab.*, Vol. 13, Issue 1, 2013, pp. 330-332.

[15]. A. Joi, R. Akolkar, U. Landau, Pulse electrodeposition of copper-manganese alloy for application in interconnect metallization, *J. Electrochemical Society*, Vol. 160, Issue 12, 2013, pp. D3145-D3148.

[16]. M. H. van der Veen, N. Heylen, O. V. Pedreira, I. Ciofi, S. Decoster, V. V. Gonzalez, N. Jourdan, H. Struyf, K. Croes, C. J. Wilson, Z. Tőkei, Damascene benchmark of Ru, Co and Cu in scaled dimensions, in *Proceedings of the International Interconnect Technology Conference (IITC'18)*, Vol. 1, Issue 1, 2018, pp. 1-3.

[17]. A. H. Fischer, A. Abel, M. Lepper, A. E. Zitzelsberger, A. von Glasow, Modelling bimodal electromigration failure distributions, *Microelectron. Reliab.*, Vol. 41, 2001, pp. 445-453.

[18]. M. H. Lin, Y. L. Lin, K. P. Chang, K. C. Su, T. Wang, Copper interconnect electromigration behavior in various structures and precise bimodal fitting, *Jpn. J. Applied Physics*, Vol. 45, Issue 2A, 2006, pp. 700-709.

[19]. J. R. Black, Electromigration-A brief survey and some recent results, *IEEE Trans. Electron Devices*, Vol. 16, Issue 4, 1969, pp. 338-347.

[20]. H. Ceric, S. Selberherr, Electromigration in submicron interconnect features of integrated circuits, *Materials Science and Engineering R*, 2011, Vol. 71, pp. 53-86.

[21]. M. E. Sarychev, Yu. V. Zhitnikov, General model for mechanical stress evolution during electromigration, *J. Applied. Physics*, Vol. 86, Issue 6, 1999, pp. 3068-3075.

[22]. J. P. Dekker, A. Lodder, J. van Ek, Theory for the electromigration wind force in dilute alloys, *Physics Review B*, Vol. 56, Issue 19, 1997, pp. 12167-12177.

[23]. I. Ciofi, Ph. J. Roussel, Y. Saad, V. Moroz, C.-Y. Hu, R. Baert, K. Croes, A. Contino, K. Vandersmissen, W. Gao, P. Matagne, M. Badaroglu, C. J. Wilson, D. Mocuta, Z. Tökei, Modelling of via resistance for advanced technology nodes, *IEEE Trans. Electron Devices*, Vol. 64, Issue 5, 2017, pp. 2306-2313.

[24]. R. S. Sorbello, Microscopic driving forces for electromigration, *MRS Online Proceedings Library*, Vol. 427, 1996, pp. 73-81.

[25]. C. S. Hau-Riege, S. P. Hau-Riege, A. P. Marathe, The effect of interlevel dielectric on the critical tensile stress to void nucleation for the reliability of Cu interconnects, *J. Applied Physics*, Vol. 96, 2004, pp. 5792-5796.

[26]. H. Zahedmanesh, P. R. Besser, C. J. Wilson, K. Croes, Airgaps in nano-interconnects: Mechanics and impact on electromigration, *J. Applied Physics*, Vol. 120, 2016, 095103.

[27]. H. Ceric, H. Zahedmanesh, K. Croes, Analysis of electromigration failure of nano-interconnects through a combination of modelling and experimental methods, *Microelectron. Reliab.*, Vols. 100-101, 2019, 113362.

[28]. N. Singh, A. F. Bower, D. Gan, S. Yoon, P. S. Ho, J. Leu, S. Shankar, Numerical simulations and experimental measurements of stress relaxation by interface diffusion in a patterned copper interconnect structure, *J. Applied Physics*, Vol. 97, Issue 1, 2004, 135391.

[29]. Z.-S. Choi, R. Mönig, C. V. Thompson, Dependence of the electromigration flux on the crystallographic orientations of different grains in polycrystalline copper interconnects, *Applied Physics Letters*, Vol. 90, 2007, 241913.

[30]. L. Arnaud, T. Berger, G. Reimbold, Evidence of grain-boundary versus interface diffusion in electromigration experiments in copper damascene interconnects, *J. Applied Physics*, Vol. 93, Issue 1, 2003, pp. 192-204.

[31]. H. Ceric, R. L. de Orio, J. Cervenka, S. Selberherr, A comprehensive TCAD approach for assessing electromigration reliability of modern interconnects, *IEEE Trans. Device Materials Reliab.*, Vol. 9, Issue 1, 2009, pp. 9-19.

[32]. S.-T. Hu, L. Cao, L. Spinella, P. S. Ho, Microstructure evolution and effect on resistivity for Cu nanointerconnects and beyond, in *Proceedings of the International Electron Devices Meeting (IEDM'18)*, 2018, pp. 5.4.1-5.4.3.

[33]. C.-K. Hu, L. Gignac, G. Lian, C. Cabral, K. Motoyama, H. Shobha, J. Demarest, Y. Ostrovski, C. M. Breslin, M. Ali, J. Benedict, P. S. McLaughlin, J. Ni, X. H. Liu, Mechanisms of electromigration damage in Cu interconnects, in *Proceedings of the International Electron Devices Meeting (IEDM'18)*, 2018, pp. 5.2.1-5.2.4.

[34]. L. E. Spinella, T. Jiang, N. Tamura, J.-H. Im, P. S. Ho, Synchrotron X-ray microdiffraction investigation of scaling effects on reliability for through-silicon vias for 3-D integration, *IEEE Trans. Device Materials Reliab.*, Vol. 19, Issue 3, 2019, pp. 568-571.

[35]. M. A. Meyer, I. Zienert, E. Zschech, Electron backscatter diffraction: Application to Cu interconnects in top-view and cross section, in Materials for Information Technology (E. Zschech, C. Whelan, Th. Mikolajick, Eds.), *Springer*, 2005, pp. 485-495.

[36]. H. Ceric, S. Selberherr, H. Zahedmanesh, R. Orio, K. Croes, Review – modelling methods for analysis of electromigration degradation in nano-interconnects, *ECS J. Solid State Science Techn.*, Vol. 10, 2021, 035003.

[37]. COMSOL Multiphysics, Version 5.4. www.comsol.com

[38]. S. Choi, C. Christiansen, L. Cao, J. Zhang, R. Filippi, T. Shen, K. B. Yeap, S. Ogden, H. Zhang, B. Fu, P. Justison, Effect of Metal Line Width on Electromigration of BEOL Cu Interconnects, in *Proceedings of the International Reliability Physics Symposium (IRPS'18)*, 2018, pp. F.4.1-F.4.6.